Yi Yang, Ching-Tai Ng and Andrei Kotousov

Influence of crack opening and incident wave angle on second harmonic generation of Lamb waves

Smart Materials and Structures, 2018; 27(5):055013-1-055013-15

Influence of crack opening and incident wave angle on second harmonic generation of Lamb waves

Yi Yang[1], Ching-Tai Ng[1,*] and Andrei Kotousov[2]

[1] School of Civil, Environmental & Mining Engineering, The University of Adelaide, Adelaide, SA 5005, Australia

[2] School of Mechanical Engineering, The University of Adelaide, Adelaide, SA 5005, Australia

[*] E-mail: alex.ng@adelaide.edu.au

Abstract

Techniques utilising second harmonic generation (SHG) have proven its great potential in detecting contact-type damage. However, the gap between the practical applications and laboratory studies is still quite large. The current work is aimed to bridge this gap by investigating the effects of the applied load and incident wave angle on the detectability of fatigue cracks at various lengths. Both effects are critical for practical implementations of these techniques. The present experimental study supported by three-dimensional (3D) finite element (FE) modelling has demonstrated that the applied load, which changes the crack opening and, subsequently, the contact nonlinearity, significantly affects the amplitude of the second harmonic generated by the (S_0) symmetric mode of Lamb waves. This amplitude is also dependent on the length of the fatigue crack as well as the incident wave angle. The experimental and FE results correlate well, so the modelling approach can be implemented for practical design of damage monitoring systems as well as for the evaluation of the severity of the fatigue cracks.

Keywords: second harmonic, nonlinear Lamb wave, contact nonlinearity, applied load, incident wave angle, fatigue crack, crack opening

1. Introduction

1.1. Lamb waves for damage detection

In the last few decades, damage detection techniques utilising guided waves [1, 2] have attracted significant attention due to its advantages over the conventional non-destructive inspection methods [3, 4]. These advantages include the ability to monitor large areas, including inaccessible locations, with a small number of inexpensive piezoelectric sensors, which can be permanently attached to the structure for continuous measurements [5, 6]. Several damage detection methods utilising either linear or nonlinear characteristics of Lamb wave propagation have been proposed in the past [7]. Most of these methods, however, are based on the linear features of Lamb waves e.g. methods utilising analysis of reflection and transmission signals [8, 9] and time-of-flight [10, 11] as well as the mode conversion phenomena [12, 13]. However, these linear methods are only capable to detect mechanical damage (e.g. fatigue cracks, delaminations and corrosion spots) with the characteristic sizes of the same order of the magnitude as the wavelength of the incident wave.

The wavelength of the incident wave cannot be too small in practical applications as the high frequency (corresponding to short wavelengths) normally generates multiple propagating wave modes, which can make the signal acquisition and analysis very challenging. The damage detection methods, which rely on the linear characteristics or phenomena of Lamb wave propagation, usually require reference or baseline data in order to extract the residual signal, which correspond to the material damage. However, it has been shown in the literature that the baseline signal can be strongly affected by the change of environmental and loading conditions leading to a significant degradation in damage sensitivity of linear methods [9, 14]. The latter is

the main reason why the methods, which perfectly work in laboratory conditions, fail to deliver the similar performance in the real-world environment.

In contrast, nonlinear features of Lamb wave are much more sensitive to incipient damage to the early state of material degradation [15]. In addition, the damage detection techniques utilising nonlinear features of Lamb wave propagation do not require the reference or baseline data (signal) to detect damage [16]. Therefore, the nonlinear methods could have a better performance and fewer limitations than their linear counterparts in the real-world environment. Recently, a number of studies attempted to apply various nonlinear features of Lamb wave propagation for damage detection, for example, higher harmonic generation phenomenon [16, 17], sidebands generation [18-20], and nonlinear resonance effects [21, 22]. The present paper focuses on the second harmonic generation (SHG) phenomenon for the contact-type damage detection, which will be briefly discussed next.

1.2. Second harmonic generation (SHG)

A distortion of the excitation wave by the clapping mechanism, which will be described below, leads to the generation of higher harmonics. During this process the wave energy from the frequency of the incident wave pumps into the second or even higher order harmonics. The process can be governed by the global material nonlinearity [15, 17, 23], or local damage-induced nonlinearity [24-26]. One of the local nonlinearity effects, contact nonlinearity [27], has recently gained an increasing attention. It is associated with contact-type damages, such as fatigue crack, delamination or debonding. The present study is concerned with the contact nonlinearity due to fatigue cracks. It manifests itself when an incident wave of sufficiently large enough amplitude interacts with a so-called “breathing crack”, which behaves like a “mechanical

diode". The compressional part of the wave closes the crack (or a section of the crack) while the tensile part tends to open the crack or its section (as fatigue cracks are normally closed due to plasticity effects near the crack tip and the wake of plasticity due to crack fatigue growth). This nonlinear phenomenon leads to the generation of a number of higher harmonics and sub-harmonics as a result of parametric modulation, which can be used for the detection and characterisation of the fatigue crack. Below we also provide a brief overview of the selected studies related to the contact nonlinearity and SHG.

Most of the simple and popular analytical approaches to model the contact nonlinearity and clapping mechanism are based on bi-linear stiffness approximation. When the crack is open, the global stiffness is reduced; when the crack is closed, the stiffness has its nominal value. Many studies in the past utilised this approach and were able to reproduce the generation of the second and higher order harmonics.

There were many studies in the past on SHG caused by contact nonlinearity [28-30], however, most of them focused on bulk waves. For example, Biwa *et al*. [31] investigated the SHG of a longitudinal wave at the contact interface of two aluminium blocks. They demonstrated that an increase of the contact pressure at the interface leads to the reduction of the second harmonic magnitude. It means that the SHG depends on the magnitude of the contact pressure, therefore, justifies the objectives of the current study. Lee and Jhang [32] investigated the SHG due to presence of fatigue cracks in an aluminium sample, using an ultrasonic wave scanning technique. A relative nonlinear parameter was utilised for the evaluation of the contact nonlinearity and avoid the effect of other nonlinearities associated with the equipment and material behaviour.

Hong *et al*. [17] examined the synchronising characteristics of high frequency Lamb wave interactions with a fatigue crack. However, investigations of the nonlinear phenomena at high frequencies need quite sophisticated equipment, instrumentation and signal processing due to the dispersive nature of Lamb waves at high frequencies. Recently, Yang *et al*. [33] investigated the SHG due to the presence of fatigue cracks using low frequency symmetric and anti-symmetric modes of Lamb waves. It appears that the fundamental symmetric mode (S_0) is promising for monitoring and evaluation of fatigue damage. Subsequently, the present study focuses on relatively low excitation frequencies, which generate only the fundamental modes of Lamb waves, and, in particular, on the S_0, which is much less dispersive than the fundamental anti-symmetric fundamental mode (A_0) of Lamb wave.

Most previous experimental and numerical studies simply ignored the effect of the applied load on the SHG. However, in many practical applications the applied loading cannot be avoided and it can change the crack opening, and hence, alter the contact conditions (contact nonlinearity) at the crack surfaces. For example, Lim *et al*. [34] demonstrated that the crack opening has a large effect on the magnitude of the SHG. Therefore, for practical applications the evaluation of the effect of the applied load on the magnitude of the SHG is essential. For this reason, it is also included as one of the objectives in the current study. Along with the mechanical phenomena, this work also focuses on the development of numerical approach for the evaluation of SHG and modelling the wave interactions and the effect of the applied loading. This is motivated by the practical considerations, where a pure experimental approach is unrealistic for the design of a fatigue crack monitoring and evaluation system. It is believed that numerical approaches will play a leading role in the development and design of damage monitoring systems, and provide much more efficient solutions to practical challenges.

The primary objective of this study is to improve the understanding of the SHG of Lamb waves due to presence of fatigue cracks under realistic conditions with a focus on the practical implementation of this technique for in-situ monitoring. The current study investigates the influence of the crack opening due to the applied loading and the incident wave angle on the SHG induced by the nonlinear interaction of fatigue cracks of various lengths with the S_0 Lamb waves.

The article is arranged as follows. A detailed description of the experimental set-up is presented in Section 2, which includes the details of the specimen preparation procedures, signal generation methods, data acquisition system. Section 3 describes the finite element (FE) modelling approach, which is used to support the experimental studies. In Section 4, the frequency selection criteria based on the mode tuning studies are outlined. The experimental results and validation of the FE model are provided in Section 5. This section also presents the results of a parametric study utilising the experimentally verified three-dimensional (3D) FE modelling approach. Finally, main conclusions of the research outcomes are presented in Section 6.

2. Experimental setup

This section first outlines the details of the specimen fabrication procedures, specifically the generation of fatigue cracks. The experimental setup for the excitation and sensing the Lamb waves is also described in this section.

2.1. Experiment specimen

A 5005-H34 aluminium plate was cut into a dog-bone shape specimen as shown in Figure 1a. The in-plane dimensions of the specimen are 400mm×300mm and the thickness is 3mm. The material properties of the plate are given in Table 1. Piezoceramic discs (Ferroperm Pz27) with 10mm diameter and 0.5mm thickness were permanently bonded to the surface of the plate specimen by a conductive epoxy. The material properties of the piezoceramic discs are also listed in Table 2. The piezoceramic discs were used to form a circular transducer network with radius R = 40mm as shown in Figure 1a. A polar coordinate system is set at the centre of the plate. Based on this reference system, all eight piezoceramic discs were located at r = 40mm and $0^{o} \leq \theta \leq 315^{o}$ with 45° interval. In this study, one of the piezoceramic discs was used to actuate the Lamb waves while the rest of the piezoceramic discs were used to sense the Lamb wave signals.

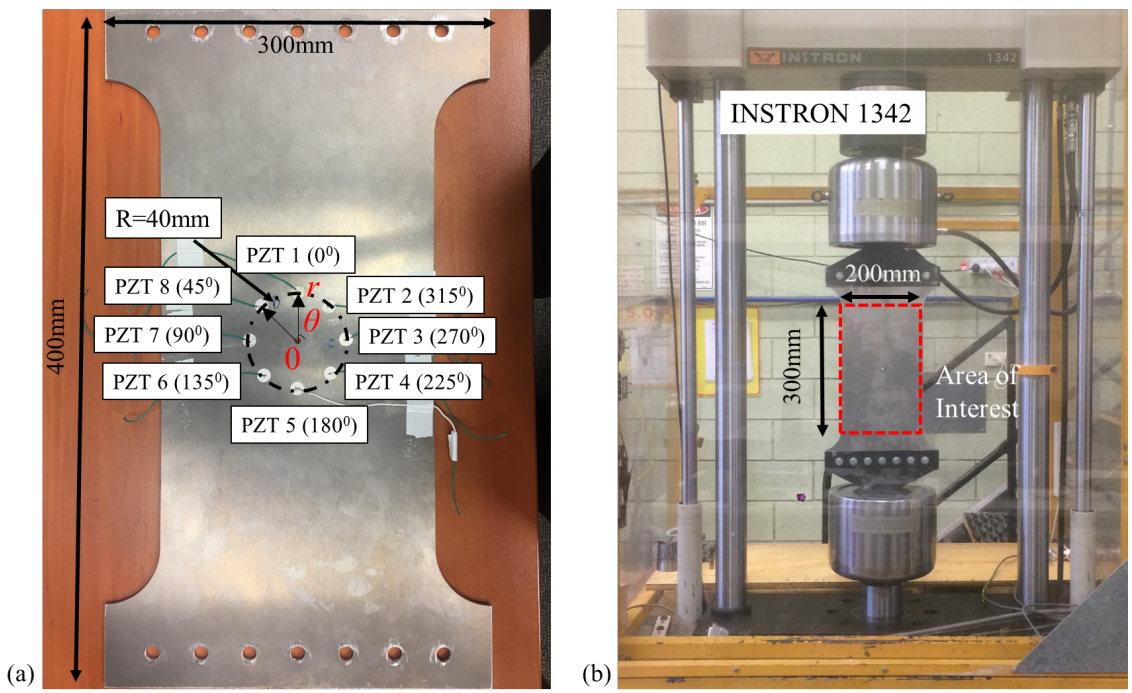

Figure 1: (a) Aluminium plate with installed piezoceramic discs and (b) cyclic loading equipment and area of interest in the specimen.

Table 1: Material properties of the 5005-H34 aluminium plate

Young's Modulus (GPa)	69.5
Poisson Ratio	0.33
Density (kg/m^3)	2700

Table 2: Material properties of the Ferroperm Pz27 Piezoceramic discs

Young's Modulus (GPa)	59
Poisson Ratio	0.389
Density (kg/m^3)	7700
Relative Dielectric Constant	1800
Piezoelectric Charge Constant (m/V)	170×10^{-12}
Permeability (F/M)	8.854×10^{-12}

2.2. Fatigue crack generation

Fatigue cracks in the aluminium sample were generated as follow. A 5mm circular through hole was first drilled at the centre of the aluminium plate to facilitate the fatigue crack initiation. Two 1mm long starter notches were cut using a 0.5mm thick saw blade in the directions θ= 90° and 270° referring to the polar coordinate system as shown in Figure 1a. The plate was then loaded cyclically under a 10Hz sinusoidal tensile load with a minimum force of 5kN and a maximum force of 30kN, as shown in Figure 1b. A fatigue crack was initiated and observed at each starter notch after 250,000 cycles. The SHG tests were performed after every 100,000 cycles. Both cracks grew to about 8mm after 800,000 cycles, which corresponds to, so called, Paris fatigue crack growth regime.

2.3. Actuating and sensing Lamb waves

A computer controlled signal generator (NI PIX-5412) was used to generate the excitation signals. The excitation signal is a narrow-band eight-cycle sinusoidal tone burst pulse modulated

by a Hanning window. A typical excitation signal has a peak-to-peak output voltage of 10V. The signal was amplified by 5 times using an amplifier (KROHN-HITE 7500) before it was sent to one of the transducers, while the rest of the transducers were used to measure the wave signal. The signals were digitized by a data acquisition system (NI PXIe-5105) and then fed into a computer. The quality and repeatability of the measurements were improved by averaging the signals with 64 acquisitions.

In this study, the measured time duration was limited to 50μs. This ensured that the recorded signals cover only the Lamb waves travelling within the area as highlighted in Figure 1b, and hence, it (the time duration) avoids the effect of the plate clamps on SHG. In practice, there are always presence of non-damage related nonlinearities, e.g. material nonlinearity of the plate, inherent nonlinearity of electrical equipment, the material coupling between transducers and surface of the plate, and background noise, etc. To avoid the contribution of these nonlinearities into the observed SHG, the wave signals were generated and measured for the intact plate (before cycling loading); and these data were used as a benchmark to ensure that the measured (during the fatigue tests) nonlinearity represents the contact nonlinearity and not the non-damage related nonlinearities.

3. Three-dimensional finite element model

A 3D FE model was created using commercial FE software, ABAQUS, to support the numerical study. Figure 2 shows schematic diagrams of the FE model including the through hole, starter notches, fatigue cracks and transducer models. The dimension of the aluminium model is 300mm×200mm, which is the same as the area of interest for the plate sample in the experiment as shown in Figure 2b. The thickness of the aluminium plate model is 3mm, which also

replicates the specimen. According to the theory [35, 36], the radial displacement on the circumference of the actuator in FE model is linearly related to the voltage applied in the experiment, and thus in FE model the excitation can be modelled by applying a radial displacement on the circumference of the PZT model. For the sensor model, the strain at the centre of the PZT is linearly related to the received voltage, so the output from the FE model can be obtained as the strain from the middle of the PZT model. In the FE model, it is assumed that the piezoceramic discs are perfectly bonded to the aluminium plate. The material properties of the plate and piezoceramic disc model are the same as the specimen in the experiment.

Eight-noded brick elements, C3D8I, in which each node has three translational degrees-of-freedom (DoFs), were used to model both the aluminium plate and the piezoceramic discs. The in-plane dimension and the thickness of the elements are around 0.4mm×0.4mm and 0.375mm, and hence, there at least 20 elements per wavelength for the incident Lamb wave and the induced second harmonic wave. There are eight layers of elements in the thickness direction of the aluminium plate. The aspect ratio of the solid elements is 1.07. An intact plate is also modelled to ensure that the second harmonic obtained from the FE model with the damage is generated by the fatigue crack. To model the experimental condition of the specimens, a 5mm diameter circular through-hole and two 1mm×1mm starter notches were modelled by removing elements for both intact and damaged plates. For the damaged plate, the fatigue crack was simulated by inserting a seam at both end of each starter notch. The crack was arranged in vertical direction as shown in Figure 2b. It should be noted that the model is meshed automatically in ABAQUS, the meshes around the through hole and notch are not perfectly symmetric about the centre of the model, and the meshes of PZT models are not symmetric as well. As a result, the wave signal obtained at the symmetric PZT pairs about the incident wave

propagation direction is not exactly the same. However, the differences are subtle and they will be shown in Section 5.

The hard normal contact and frictional tangential contact were applied to the interfaces of the seam crack to prevent nodes penetration, and hence, simulating the clapping of the crack interfaces when the Lamb waves propagate through the fatigue cracks. An increased value of the friction coefficient of 1.5 [37] was used to account for the increased friction due to the roughness of the actual crack surfaces, crack tip plasticity and plasticity–induced crack closure effects associated with fatigue crack propagation. This value was found empirically as the best fit to the experimental data. The transient problem was solved using the explicit FE code, ABAQUS/Explicit, which employs the explicit central different integration scheme to calculate the response of the wave propagation.

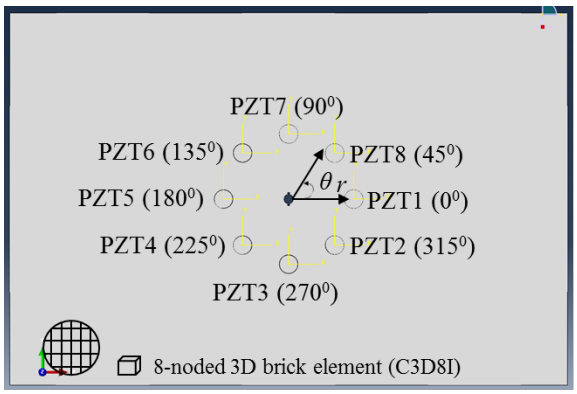

(a)

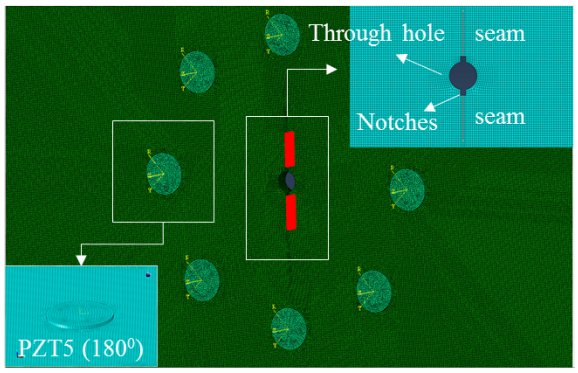

(b)

Figure 2: Schematic diagram of (a) the finite element model, and (b) the model of the fatigue cracks and piezoceramic transducer.

4. Lamb wave mode tuning procedure

In the beginning of the experimental study, mode-tuning experiments [38, 39] were carried out to determine the excitation frequency that could generate S_0 dominated signal. The S_0 Lamb wave is selected as the incident wave in this study as this mode is more sensitive to the fatigue crack than the A_0 Lamb wave [33]. This was briefly discussed in the Section 1. In the low frequency region, both S_0 and A_0 Lamb wave are normally excited simultaneously. Thus, a pair of the piezoceramic discs were attached to the surface of a larger aluminium plate (1m×1m) with the same material properties and thickness as the plate used in the fatigue test. The narrow-band sinusoidal tone burst pulse modulated by a Hanning window was applied to one of the piezoceramic discs to generate the dominant S_0 Lamb wave mode. The excitation frequency was swept from 10kHz to 400kHz. At the same time, the other piezoceramic discs were used to measure the Lamb wave signals. At each excitation frequency, the amplitude ratio of S_0 to A_0 Lamb wave were recorded. Figure 3 shows the Lamb wave mode-tuning results. According to the results, the maximum amplitude ratio of the S_0 to A_0 Lamb waves is at 240kHz. Therefore, the excitation frequency of 240kHz was chosen to excite the S_0 dominated Lamb wave in the experimental studies. From the current results, the maximum amplitude ratio of the S_0 to A_0 Lamb waves is at 240kHz. Although the thickness and material properties of the specimen are slightly different, the optimal frequency obtained in the current study is comparable to the results from the previous study [38], where it was found to be between 230kHz and 330kHz.

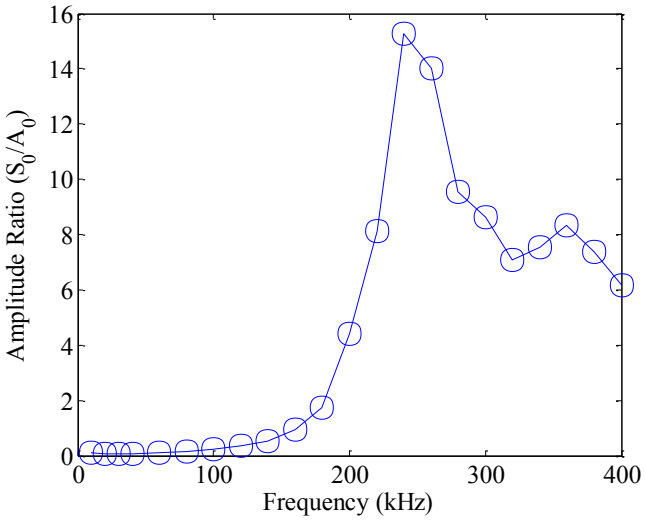

Figure 3: Ratio of S_0 to A_0 Lamb wave amplitude excited on the aluminium plate using a 10mm diameter and 0.5mm thick Ferroperm Pz27 piezoceramic disc.

5. Results and discussion

The influence of the incident wave angle and crack opening due to the applied load on the SHG due to presence of fatigue cracks was investigated using experimental and 3D FE modelling approaches. The accuracy of the FE model in predicting the SHG was validated by comparing the simulation results with the experimental data. The experimentally validated 3D FE model is then used to obtain directivity patterns of the SHG with the consideration of different incident wave angles and crack openings due to the applied load.

5.1. Second harmonic generation (SHG) at the fatigue crack

Short Time Fourier Transform (STFT) was used to transform all of the acquired time series data to the time-frequency domain because it is easier to distinguish the first arrival wave signals from the boundary reflections. The spectrogram parameters in the STFT were carefully selected by a series of trials to ensure the balance between time and frequency resolution.

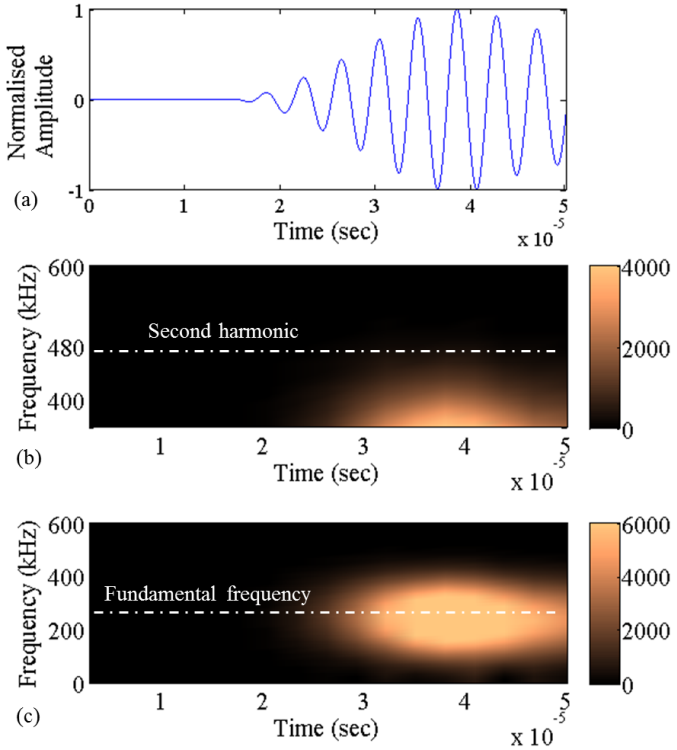

Figure 4: Spectrogram of the FE results for PZT1 with 240kHz excitation frequency for an intact model, (a) time domain signal, (b) second harmonic frequency range, and (c) incident wave frequency range.

Figure 4 shows the spectrogram of the Lamb wave signal captured at PZT1 in the FE simulation for an intact model. Different to other FE simulation results, an incident wave with a larger displacement magnitude (100μm) is used to provide a better illustration of the wave distortion due to contact nonlinearity at the fatigue cracks. As shown in Figure 4b, there is no visible energy at the second harmonic frequency (double of the excitation frequency). While for the damaged plate, i.e. a model with an 8mm fatigue crack at each of the starter notch (hole), the time-domain signal as shown in Figure 5a is distorted as compared with the intact plate (Figure 4a), especially for the tensile part of the wave. As shown in the spectrogram in Figures 5b and 5c, it is clear that the wave energy is transmitted from the fundamental frequency to second harmonic frequency when the fatigue crack presents in the model. For the intact plate (Figure 4b),

the second harmonic is negligible as compared with the result of the damaged plate as shown in Figure 5b. In contrast, in experimental studies, the second harmonic might be not negligible for the intact plate as it can also be generated from the coupling between the transducers and host plate, signal generator and data acquisition system.

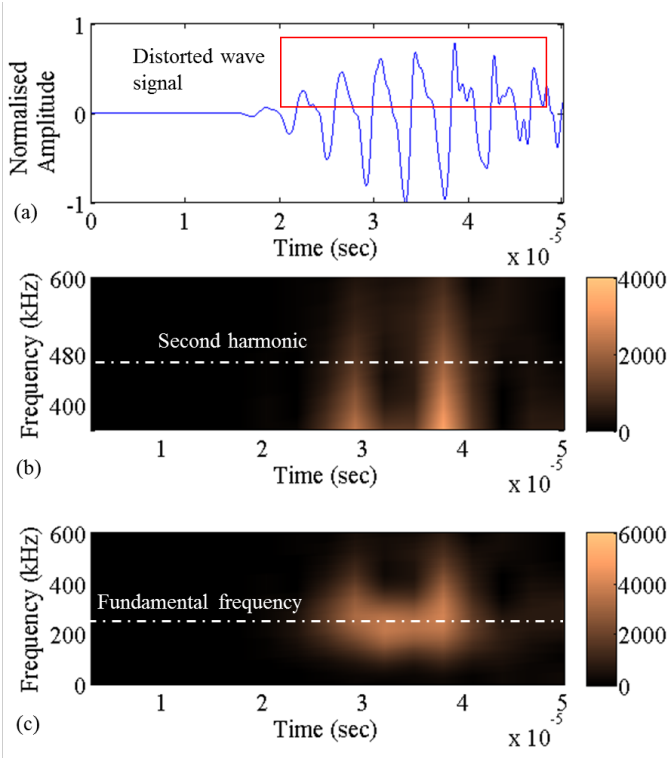

Figure 5: Spectrogram of FE results for PZT1 240kHz excitation frequency for the model with fatigue cracks, (a) time domain signal, (b) second harmonic frequency range, and (c) incident wave frequency range.

The experimental amplitude profile of the spectrogram at 240kHz and 480kHz were extracted for the intact and damaged plate. The results are normalized by the maximum value of the wave signal at the fundamental frequency. The group velocities of the S_0 Lamb wave at these two frequencies are almost the same. Figures 6 and 7 show the amplitude profile of the signal at the excitation frequency and second harmonic frequency for intact and damaged plate, respectively. In these figures, the arrival time of the wave signal is marked using a vertical

dashed line. The arrival time of the wave pulse at the excitation frequency is the incident wave propagates directly from the actuator to the sensor. In practice, the second harmonic wave also exists in the intact specimen due to different factors, such as nonlinearity of the equipment and material nonlinearity of the specimens in the experiment. The second harmonic wave due to the aforementioned non-damage related nonlinearities should arrive at the same time as the wave pulse at the excitation frequency and this agrees with the results as shown in Figure 6.

Figure 7 displays that the magnitude of the second harmonic is higher than that in Figure 6 (intact sample). Figure 7 also shows that the second harmonic wave due to the contact nonlinearity in the damaged sample arrives after the incident wave at the excitation frequency for PZT2, PZT3 and PZT4. This is due to the fact that the arrival time of the second harmonic wave is the time of the incident wave propagates from the actuator to the fatigue crack, and then the induced second harmonic wave propagates from the fatigue crack to the sensor. Since this wave path is longer than the direct wave path between the actuator and sensor of the incident wave at the excitation frequency, there is a time delay between the arrival times of the wave at the excitation frequency and second harmonic frequency. For PZT1, as the crack is at the direct wave path of the wave propagation direction, the second harmonic and excited wave arrive almost at the same time.

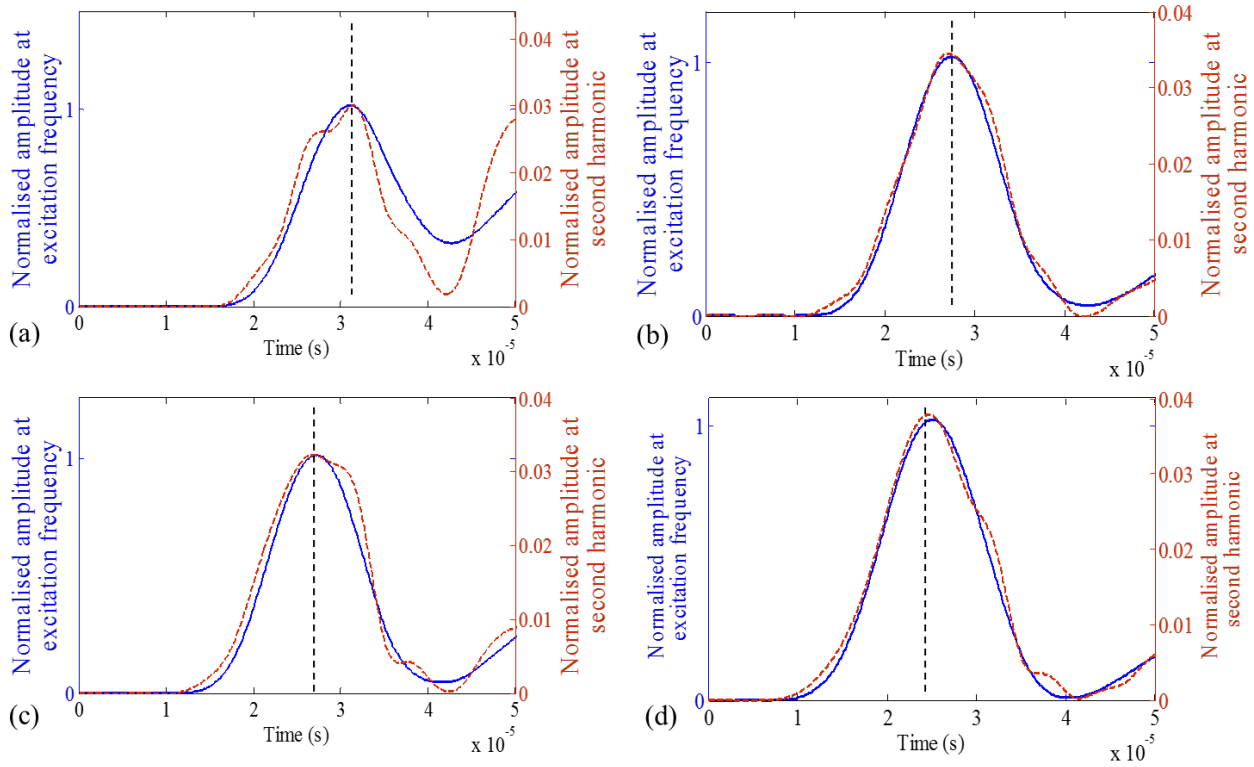

Figure 6: Experimentally measured amplitude profile at excitation frequency (blue solid lines) and second harmonic frequency (red dashed lines) for the intact plate, data measured by (a) PZT1, (b) PZT2, (c) PZT3 and (d) PZT4.

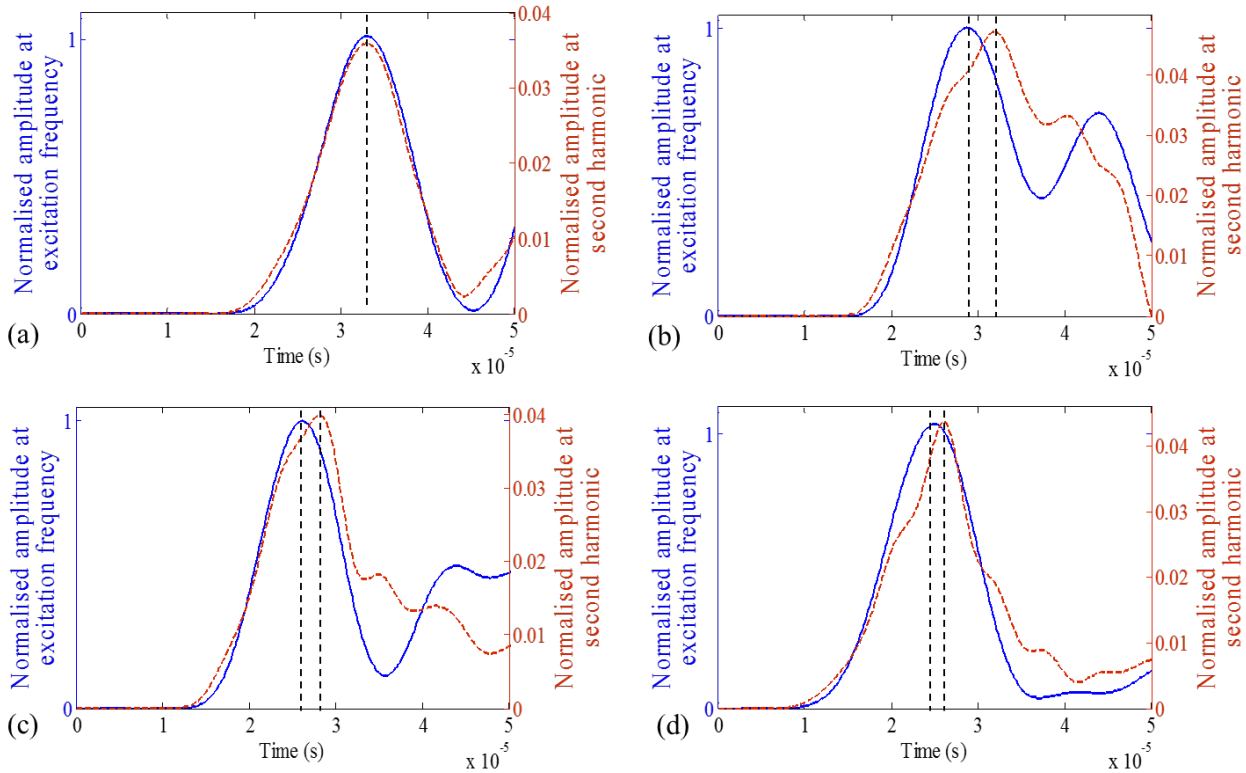

Figure 7: Experimentally measured amplitude profile at excitation frequency (blue solid lines) and second harmonic (red dashed lines) after 800,000 cycles of loading, data measured by (a) PZT1, (b) PZT2, (c) PZT3 and (d) PZT4.

5.2. Relative second order nonlinear parameter

In this study, the results are presented using the normalized relative second order parameter $\overline{\beta}'$, [32, 33] which is defined as β' normalized by the mean of β' obtained from all the cases considered in each study. Thus, β' is defined as

$$\beta' = \frac{A_2}{A_1^2} \tag{1}$$

where A_2 is the amplitude of the first peak of the amplitude profile at the second harmonic frequency (red dashed lines in Figures 6 and 7) obtained by STFT in Section 5.1, and A_1 is the first peak of the amplitude profile at the excitation frequency (solid lines in Figures 6 and 7).

5.3. Effects of the incident wave angle on the second harmonic generation (SHG)

In practical situation, the crack orientation may be different with respect to the incident wave, thus, leading to different types of the wave-crack interaction, such as opening-closing, tearing and sliding motions [20]. In the first part of this section, the variations of $\bar{\beta}'$ against crack lengths with three different incident angles are discussed together with the outcomes of the FE simulations and experimental results. It should be noted that, in practical situation, there is always a discrepancy between the radial displacements generated by the actuator in the experiments and FE simulations. Several numerical tests have been conducted to confirm that the normalised nonlinear parameter $\bar{\beta}$, which is due to the contact nonlinearity only, is independent to the amplitude of the excitation signal for a wide range of crack lengths. Therefore, for convenience of the normalisation, and in order to improve the accuracy of the numerical simulations, which might be compromised by the rounding errors, the magnitude of the excitation signal was set at 1 μm for the FE simuulation in this section.

The incident wave angles considered in this study are 90°, 45° and 0° corresponding to the incident waves generated by PZT3, PZT4 and PZT5, respectively. The experimentally measured and numerically calculated $\bar{\beta}'$ for the above incident wave angles are shown in Figures 8, 9, and 10, respectively. To ensure the consistency of the obtained $\bar{\beta}'$, the results of each pair of transducers, which are located symmetrically about the incident wave angle and crack orientation, are shown in Figures 8, 9 and 10. For 90° incident wave angle (Figure 8), the transducer pairs are PZT2 and PZT4, PZT1 and PZT5, and PZT6 and PZT8. For 0° incident wave angle (Figure 10), the transducer pairs are PZT4 and PZT6, PZT3 and PZT7, and PZT2 and PZT8.

As shown in Figures 8 and 10, i.e. the results of incident wave angle 90° and 0°, respectively, the variation of $\overline{\beta}'$ for the results of each transducer pair is very similar to each other. This is because the crack profile, i.e., the size and shape, at both sides of the through hole are also symmetric about the incident wave angle. Also, the magnitudes of the stresses induced by the applied cyclic load at both sides of the through hole are similar given the symmetric configuration of the plate and through hole with starter notches. Although these aforementioned conditions were used in the FE simulations, a very small discrepancy is observed between the results of the two transducers in each transducer pair as illustrated in Figures 8 and 10. This is because the meshing of the FE model is not perfectly symmetric about the incident wave angle and crack orientation.

The experimental results represented by the solid lines in Figures 8 and 10 also demonstrate a good agreement between the symmetric transducer pairs. However, as expected, the agreement is not as good as that in the numerical simulations. This is because the fatigue cracks at both sides of the through hole are not initiated simultaneously and, generally speaking, do not propagate symmetrically. Also, the unavoidable eccentricity of the applied load in the experiment may also cause the non-symmetric stress distribution in the plate. All these factors were the contributors to the discrepancies between the experimental studies with symmetric transducer pairs and differences between the experimental and FE results.

For 45° incident wave angle (Figure 9), although the transducer pairs of PZT3 and PZT5, PZT2 and PZT6, and PZT1 and PZT7 are located symmetrically about the incident wave angle, they are not located symmetrically about the crack orientation. The results between the transducers of each transducer pair behave quite differently due to the violation of the symmetric condition.

Overall, for the experimental and numerical results shown in Figures 8, 9 and 10 are in a good agreement in terms of the variation pattern of parameter $\bar{\beta}'$. The results for 90° incident wave angle show a better agreement with the FE results than the results of the other two incident wave angles. For the incident wave angle is 0° (Figure 10), the value of $\bar{\beta}'$ has a clear growing trend at all transducers; and the growth is more significant at PZT1, PZT2 and PZT8, i.e. the forward scattering directions. This means that under this condition, the transducers located in any direction are able to provide a warning signal for the presence of fatigue crack. However, for the cases of incident wave angle 90° (Figure 8) and 45° (Figure 9), $\bar{\beta}'$ only increases slightly with crack length to incident wave wavelength ratio and then stays about the same magnitude at most of the transducers. Noticeably for PZT2 and PZT4 of the case considering incident wave angle 90° and PZT3 and PZT5 of the case considering incident wave angle 45°, the nonlinear parameter even shows decreasing trend when the crack length to incident wavelength ratio increases. The results show that the incident wave angle plays a vital role in SHG and thus it is important to use distributed transducer networks in damage detection and monitoring of the structures.

Based on the results presented in Figures 8, 9 and 10, $\bar{\beta}'$ has different characteristics for different crack length to incident wave wavelength ratios. This means that these characteristics can be potentially used for quantitative damage identification. However, the variations of $\bar{\beta}'$ under different incident angle conditions are very different to each other. This means that the wave-crack interaction characteristic highly depends on incident wave angle. Therefore, it is essential to take into account the incident wave angle if it is used for quantitative damage identification.

In the current study, the focus is on revealing the potential influence of the incident wave angle and external loads on the features of SHG, so only one sample specimen was used in the experiment. To practically employ the SHG in detecting fatigue cracks, it is recommended to verify the repeatability of the measured SHG and this requires calibration to compensate the variation of nonlinear parameter because of the fatigue crack profiles generated in the fatigue test are different for each specimen.

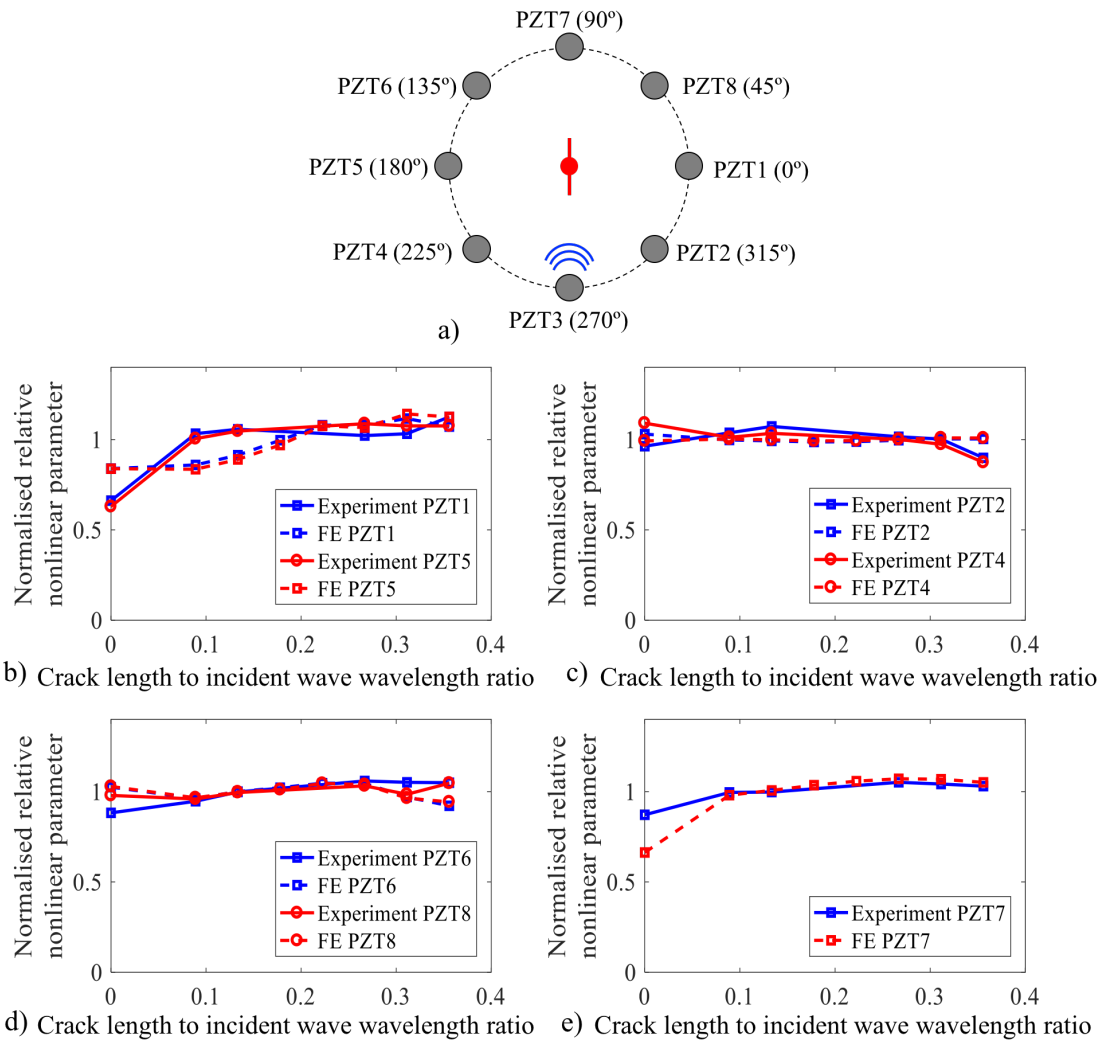

Figure 8: a) Schematical diagram of the transducer arrangement for incident wave angle 90° case, b)-e) normalized relative second order nonlinear parameter $\overline{\beta}'$ as a function of crack length to incident wave wavelength ratio at different PZTs

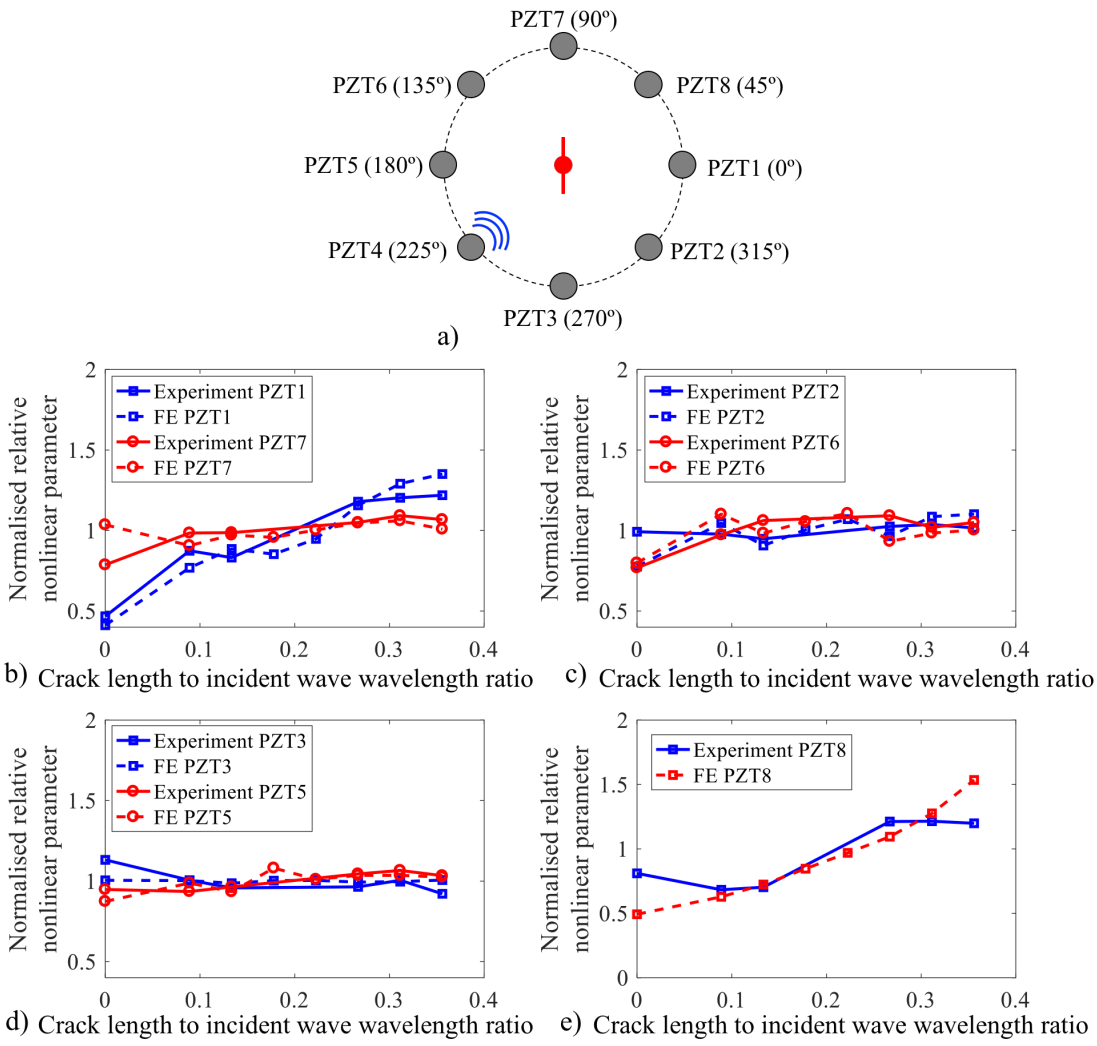

Figure 9: a) Schematical diagram of the transducer arrangement for incident wave angle 45° case, b)-e) normalized relative second order nonlinear parameter $\overline{\beta}'$ as a function of crack length to incident wave wavelength ratio at different PZTs

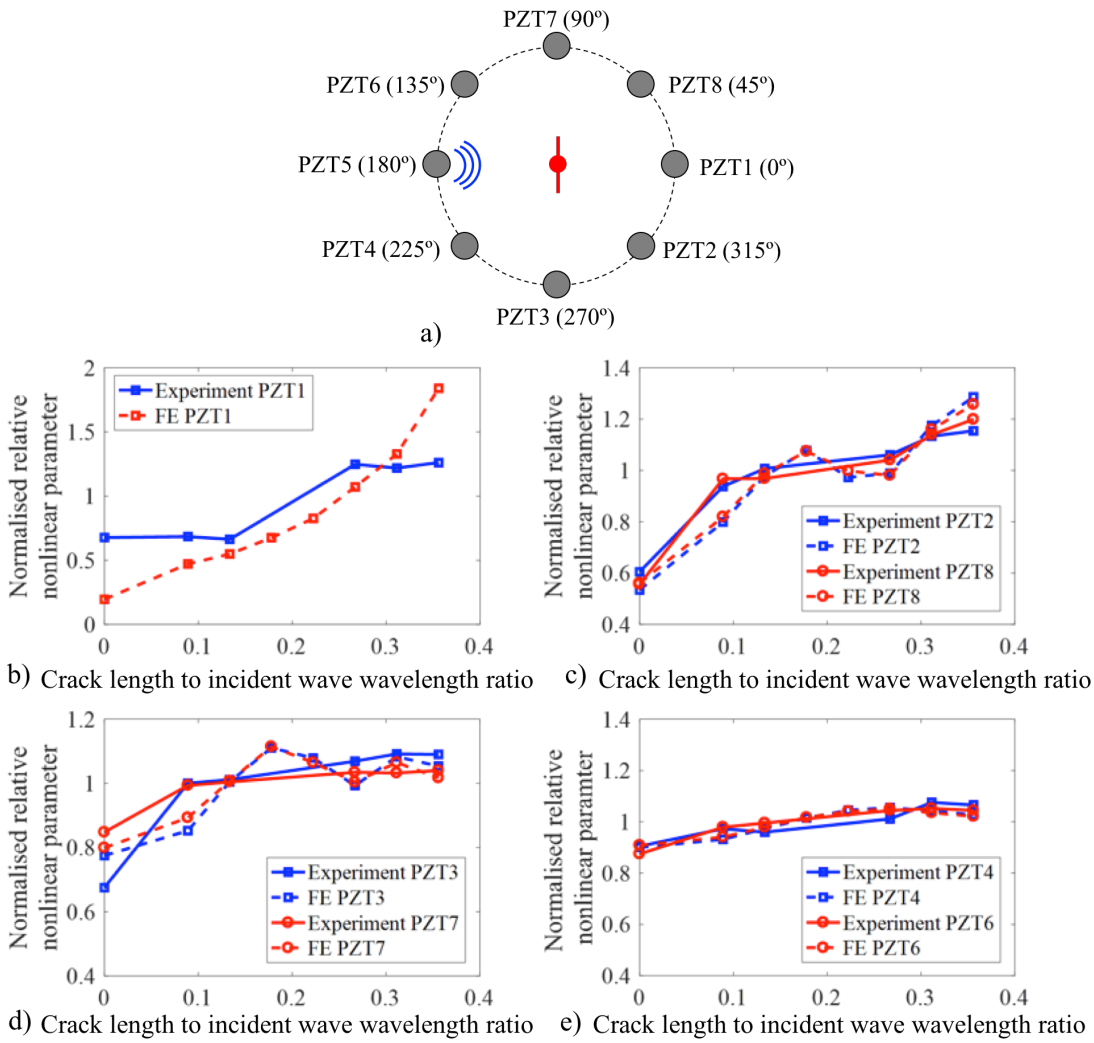

Figure 10: a) Schematical diagram of the transducer arrangement for incident wave angle 0° case, b)-e) normalized relative second order nonlinear parameter $\overline{\beta}'$ as a function of crack length to incident wave wavelength ratio at different PZTs

5.4. Second harmonic generation (SHG) at fatigue crack with different crack openings

The other issue that needs to be considered for practical application of the nonlinear Lamb wave method is that, the structure is usually subjected to changing loading conditions. These conditions can change the crack opening or the gap between the surfaces of the fatigue cracks as shown in Figure 11, and hence, it changes the properties of the contact nonlinearity. In this

section, the influence of the crack opening due to the applied loading is studied experimentally. The FE model is also adopted to support the experimental study and analyse the trends of $\overline{\beta}'$ as a function of the applied tensile stress.

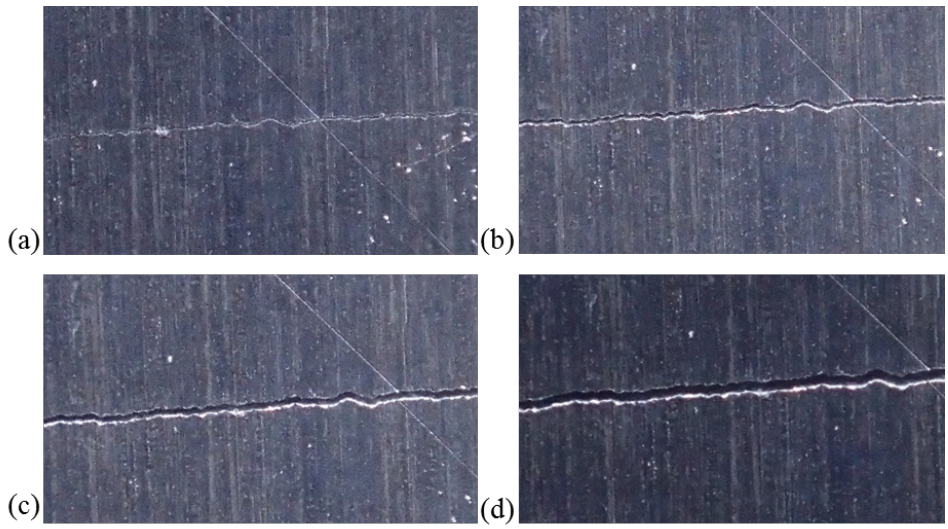

Figure 11: Crack opening under (a) 25MPa, (b) 50MPa, (c) 75MPa and (d) 100MPa tensile stress in experiments

5.4.1. Experimental observations.

The tensile load is raised from 25MPa to 100MPa to gradually increase the opening of the fatigue cracks. There are several reasons that can cause the variation of $\overline{\beta}'$ when the crack is opened due to the tensile load.

1. When the applied tensile loading increases, the distance between the crack surfaces could grow beyond the maximum in-plane displacement of the wave. The wave cannot pass through the crack, and there is no contact the crack surfaces. Thus, only small amplitude of second harmonic can be generated at the tips of the fatigue crack [34].

2. As the crack opens, it behaves like a notch when there is no contact nonlinearity. The value of $\overline{\beta}'$ can be dominated by the value of A_1 as only a small nonlinearity is generated at the crack tips due to plasticity. The value of A_1 is significantly affected by the scattering feature of linear Lamb waves at notch [40].
3. The tensile load applied on the plate would change the phase and group velocity of the propagating wave [41]. As the linear wave scattering feature at notch is relevant to the wavelength [40], variation of phase velocity will change the wavelength of the Lamb waves, and hence, change the magnitude of A_1 measured at different transducers. However, the variation of the phase velocity is usually very small and this will only cause a minor change of the magnitude of A_1.
4. For the plate used in the experiment, the ratio between the diameter of the notch and width of the plate is 0.025. According to the equation for calculating the stress concentration factor on a finite-width plate under uniaxial loading [41], the stress concentration factor at the notch in this study is around 3. When the stress applied on the plate is greater than 75MPa, the stress at the notch is around 225MPa. Considering the yielding stress of the 5005 H34 aluminium is around 145MPa – 185MPa, the area around the notch can undergo plastic deformation, and thus, increases the plasticity driven nonlinearity [23].

Figure 12 shows the experimentally measured results at PZT1 to PZT4 on the plate with the open crack after 800,000 cycles of loading in the cyclic test. The results indicate that different crack openings caused by different magnitude of applied tensile loads on a damaged structure can change the magnitude of $\overline{\beta}'$. According to Figure 12, $\overline{\beta}'$ at PZT2 and PZT3

decreases with the magnitude of the tensile load, though the variation is comparably small. At PZT4, the value of $\overline{\beta}'$ decreases when the stress is increased from 25MPa to 50MPa. Then the value increases from 50MPa to 75MPa before it drops slightly when the load is increased to 100MPa. As compared, $\overline{\beta}'$ increases at PZT1 when the stress increases from 25MPa to 75MPa, followed by a slight fall when the load reaches 100MPa.

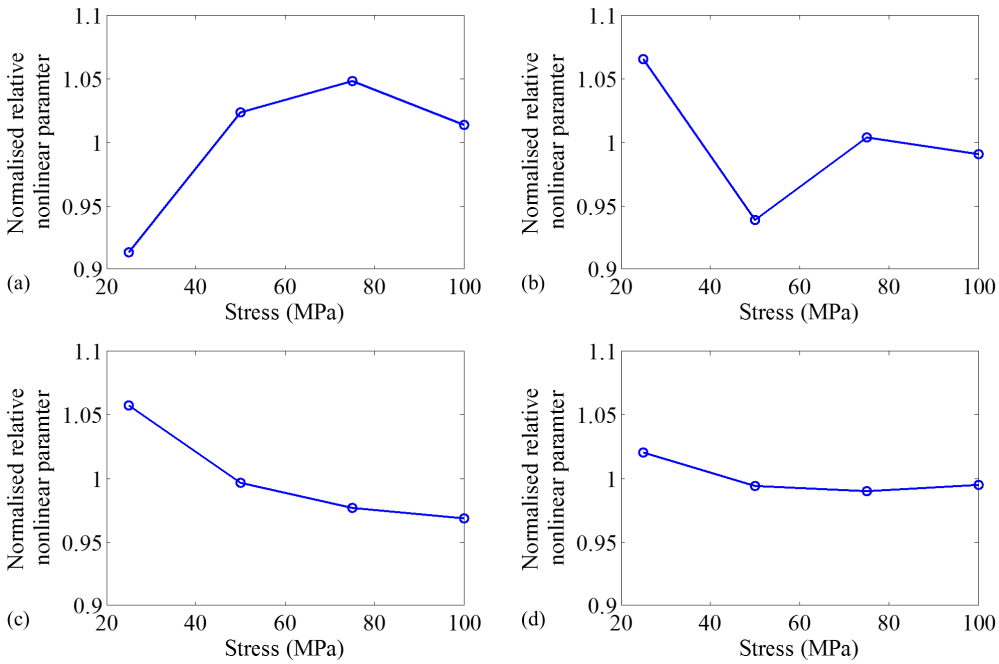

Figure 12: Experimentally measured normalized relative second order nonlinear parameter $\overline{\beta}'$ at (a) PZT1, (b) PZT2, (c) PZT3 and (d) PZT4 under different magnitudes of tensile stresses.

5.4.2. Effect of crack opening on contact nonlinearity due to presence of fatigue crack.

The experimentally verified FE model was used to study the effect of the crack opening on the contact nonlinearity. In this study, only the effect of crack opening variation was considered, which takes into account the first two reasons described in the Section 5.4.1 in causing the variation of $\overline{\beta}'$.

The fatigue crack in the FE simulations was opened by the applied tensile force at both ends of the plate. An example of the FE simulation snapshot of the stress distribution is shown in Figure 13. The results correspond to an 8mm long fatigue crack at the end of each starter notch and a 25MPa tensile stress is applied to the one end of the plate. The tensile stress with magnitudes of 8MPa, 16MPa, 25MPa, 50MPa, 75MPa and 100MPa were applied to the model. For the 25MPa stress, the maximum opening near the hole was around 9μm. When the magnitude of the tensile stress is increased to 100MPa, the opening increases to around 30μm.

The outcomes of the pre-loading steps as described above were then used to simulate the wave propagation with ABAQUS/Explicit. The maximum magnitude of the displacement applied to the actuator model was carefully controlled to ensure that the in-plane displacements of the incident wave were smaller than the smallest opening.

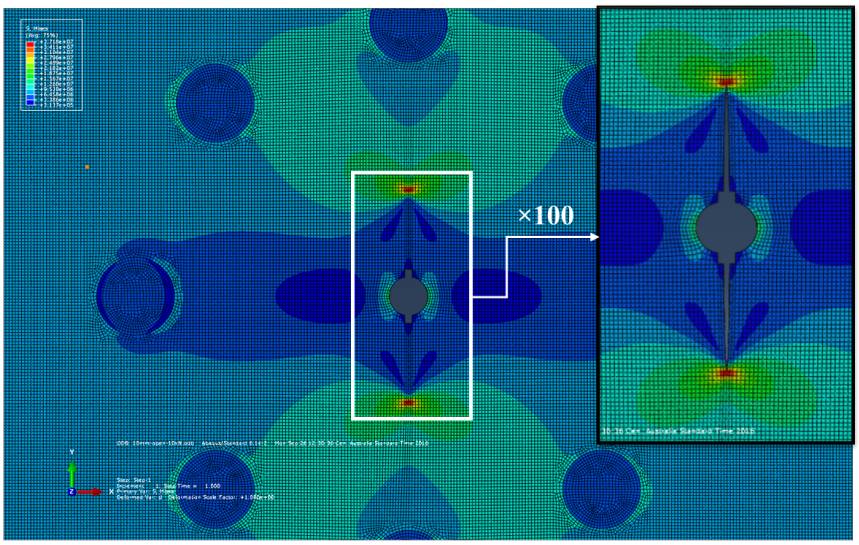

Figure 13: Fatigue cracks at both end of the FE plate model opened by 25MPa tensile stress and the stress distribution in the plate

As shown in Figure 14, for PZT1 and PZT2, there is a clear drop of the value of $\overline{\beta}'$ when the stress is increased from 8MPa to 25MPa. When the load keeps increasing, there is no clear change of the value as there is little interaction between the crack surfaces. When zooming into the variation of $\overline{\beta}'$ from 25MPa to 100MPa, a slight increase of the value is observed at PZT1, while the value at PZT2 decreases. The very small variation of $\overline{\beta}'$ can be caused by the change of scattering feature of linear Lamb waves and thus change the amplitude of A_1. In comparison, at PZT3 and PZT4, there is no distinctive variation of $\overline{\beta}'$ despite the increase of the applied tensile load.

Similar to the experimental observation, there is a distinctive cut-off point in the results of the FE simulations, beyond which there is a very small variation of $\overline{\beta}'$. In the experiments, the fatigue crack was initially open, and thus there was no sharp drop of the contact nonlinearity when the fatigue crack was pulled to reach a larger opening. For the fully opened cracks, the

variation of $\overline{\beta}'$ at different PZTs was relatively larger in experimental results than in the numerical simulations. The outcomes in these two sections indicate that when the fatigue crack is progressively opened by the applied stress (load), the variation of $\overline{\beta}'$ is mainly due to the decrease of the contact nonlinearity.

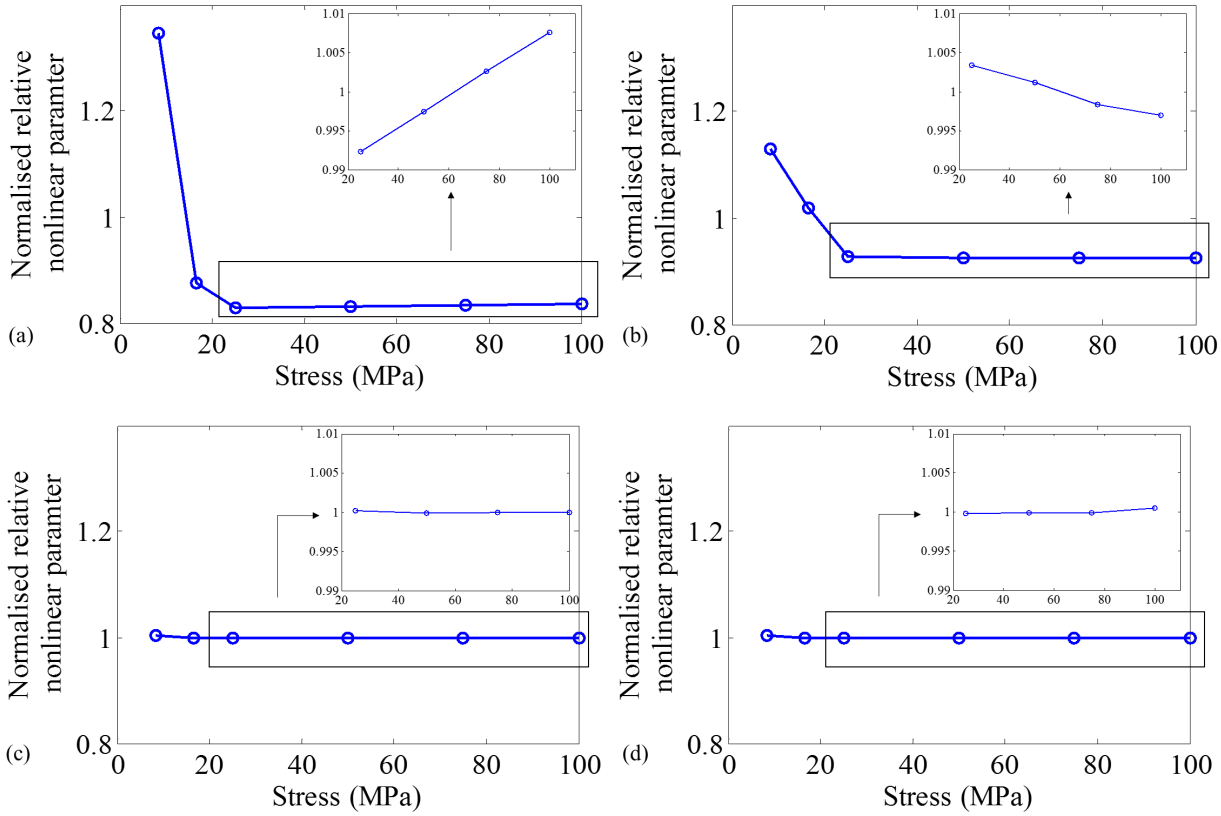

Figure 14: Numerically prediction of normalized relative second order nonlinear parameter $\overline{\beta}'$ at a) PZT1; b) PZT2; c) PZT3 and d) PZT4 on the plate model with different crack opening.

5.4.3 Directivity pattern of normalized relative second order nonlinear parameter predicted by FE simulations

It is of a great interest to investigate the directivity patterns of $\overline{\beta}'$ around a fatigue crack with different incident angles and crack openings, because these two factors directly related to the

potential practical implementation of the SHG techniques. The experimental studies of the combined effect are costly and time-consuming. Consequently, the FE approach, which has been partially validated experimentally, was used to study the directivity pattern of $\overline{\beta}'$ at fatigue crack with different crack openings and incident wave angles. It should be noted that the material and plasticity-driven nonlinearity were not modelled as the focus of this study is mainly on the loss of contact nonlinearity as a result of the applied loading.

In the parametric study, three additional transducers were added at θ = 180°, 135°, and 90° in the FE model and each of which is used as an actuator to generate incident wave at 0°, 315° (equivalent to 45°) and 270° (equivalent to 90°), respectively. The actuators were 70mm away from the crack, which is outside the circular transducer network. Only the fatigue crack is modelled at the centre of the plate, i.e. without the through-holes and starter notches. The maximum displacement applied to the circumference of the actuator model for generating the Lamb wave signal was 30μm.

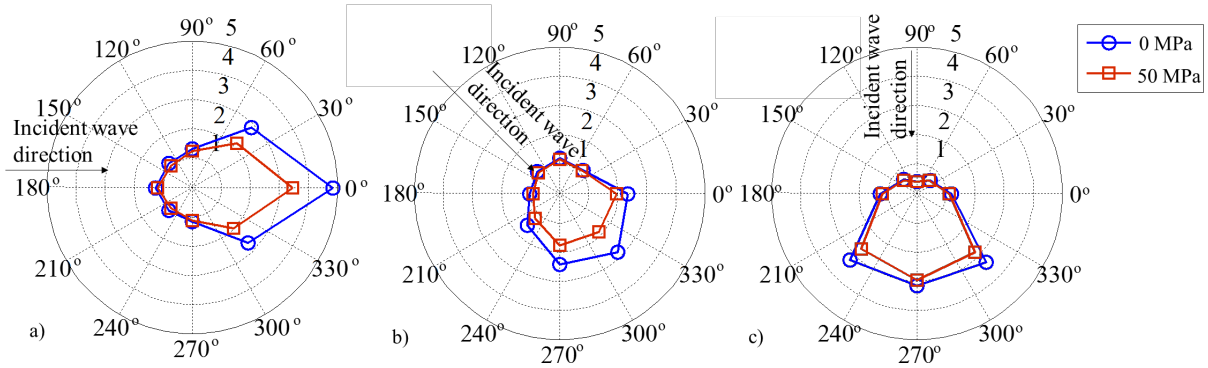

Figure 15: Directivity pattern of the normalized relative second order nonlinear parameter $\overline{\beta}'$ calculated by the FE simulation with a 16mm long fatigue crack opened by different applied tensile stresses, a) 0°, b) 315° (equivalent to 45°) and c) 270° (equivalent to 90°) incident wave angle.

Different to the aforementioned studies, the value of the normalized relative second order nonlinear parameter $\overline{\beta}'$ at each transducer is defined as β' normalized by the β' of this transducer obtained from the intact plate in this section. The outcomes of the simulations are shown in Figure 15. It can be seen that for all incident wave angles, the value of the $\overline{\beta}'$ generally shows a forward scattering pattern. However, it should be noted that for the 315° and 270° incident wave angles, the directivity patterns are slightly different to the case of 0° incident wave. The differences of the $\overline{\beta}'$ value between different angles are not as obvious as for case of 0° incident wave angle. In all these three cases, the value of $\overline{\beta}'$ is generally smaller when the crack is opened, though the directivity patterns for each case under different loads are about the same. The results indicate that clapping contact of the fatigue crack surfaces generates a relative large magnitude of second harmonic. As $\overline{\beta}'$ is generally smaller for the 315° and 270° incident wave angles, this means that the contact nonlinearity is weaker for these two cases. Overall the results show that the tensile load reduces the interaction between the crack surfaces as compared with the fully closed crack. This conclusion is also supported by previous studies, which have been briefly reviewed in the Introduction section.

6. Conclusions

This paper is devoted to the SHG due to the interactions of S_0 incident Lamb wave with fatigue cracks. The study has focused on two practical aspects relevant to in-situ damage detection, i) the effect of crack opening due to applied load and ii) different incident wave angles. It was

demonstrated experimentally that the 3D FE simulation is capable to predict the main tendencies of SHG due to the contact nonlinearity in the presence of fatigue cracks with different crack openings and incident wave angles.

The conducted study found that the magnitude of $\overline{\beta}'$ varies significantly with the incident wave angles even for the measured data obtained from the same transducer. The variation is caused by the change in contact nonlinearity, linear wave scattering and plasticity driven nonlinearity when the cracked sample is subjected to tensile loading. The observations from the experimental and FE results indicate that when the crack is progressively loaded, the variation of $\overline{\beta}'$ is mainly due to the loss of the contact nonlinearity. When the loading grows further, the increase of the nonlinearity can be associated with the plasticity mechanisms. From the present results, it is also found that the variation of $\overline{\beta}'$ was mainly dominated by the contact nonlinearity due to the increase of the fatigue crack length under the same applied load.

A number of case studies have been conducted using the validated FE approach to investigate the directivity patterns of $\overline{\beta}'$ under different incident wave angles and crack openings. The results show that the incident wave angles and applied loads on the plate could significantly change the SHG behaviour. It is important that these two important factors need to be taken into consideration in the potential applications of the techniques based on SHG for in-situ damage detection of fatigue cracks.

Acknowledgements

This work was supported by the Australian Research Council (ARC) under Grant Numbers DP160102233 and DE130100261. The supports are greatly appreciated.

References

[1] Haynes C, Todd M 2015 *Mech. Syst. Signal. Process.* **54-55** 195-209

[2] He S, Ng CT 2016 *Eng. Struct.* **127** 602-14

[3] Rose JL 2002 *J. Press. Vessel. Technol.* **124** 273-82

[4] Raghavan A, Cesnik C 2007 *Shock and Vibration Digest* **39** 91-114

[5] Farrar CR, Worden K 2007 *Phil. Trans. R. Soc. A* **365** 303-15

[6] Giurgiutiu V 2015 *Structural Health Monitoring of Aerospace Composite* (Academic Press)

[7] Mitra M, Gopalakrishnan S 2016 *Smart. Mater. Struct.* **25** 053001

[8] Ng CT 2015 *Int. J. Struct. Stab. Dyn.* **15** 1540010

[9] Aryan P, Kotousov A, Ng CT, Cazzolato BS 2017 *Struct. Contr. Health Monitor.* **24** e1894

[10] Clarke T, Cawley P, Wilcox PD, Croxford AJ 2009 *IEEE Trans. Ultrason. Ferroelectr. Freq. Control* **56** 2666-78

[11] Sikdar S, Banerjee S 2016 *Compos. Struct.* **152** 568-78

[12] Zhang J, Drinkwater BW, Wilcox PD, Hunter AJ 2010 *NDT&E Int.* **43** 123-33

[13] He S and Ng CT 2017 *Mech. Syst. Signal Process.* **84** 324-45

[14] Aryan P, Kotousov A, Ng CT, Wildy S 2016 *Smart Mater. Struct.* **25** 035018

[15] Bermes C, Kim JY, Qu J, Jacobs LJ 2008 *Mech. Syst. Signal Process.* **22** 638-646

[16] Soleimanpour R, Ng CT 2017 *Eng. Struct.* **131** 207-19

[17] Hong M, Su Z, Wang Q, Cheng L, Qing X 2014 *Ultrasonics.* **54** 770-78

[18] Zagrai A, Donskoy D, Chudnovsky A, Golovin E 2008 *Res. Nondstruct. Eval.* **19** 104-28

[19] Yoder NC, Adams DE 2010 *Struct. Health Monitor.* **9** 257-67

[20] Klepka A, Staszewski WJ, Jenal RB, Szwedo M, Iwaniec J, Uhl T 2011 *Struct. Health Monitor.* **11** 197-211

[21] TenCate JA, Smith E, Guyer RA 2000 *Phys. Review Letter.* **85** 1020-23

[22] Chondros TG, Dimarogonas AD, Yao J 2011 *J. Sound Vib.* **239** 57–67

[23] Pruell C, Kim JY, Qu J, Jacobs LJ 2009 *NDT&E Int.* **42** 199-203

[24] Jhang KY 2009 *Int. J. Precis. Eng. Man.* **10** 123-35

[25] He S, Ng CT 2017 *Smart Mater. Struct.* **26** 085002

[26] Soleimanpour R, Ng CT, Wang CH 2017 *Struct. Health Monit.* **16** 400-17

[27] Solodov I, Krohn N, Busse G 2002 *Ultrasonics.* **40** 621-25

[28] Scarselli G, Ciampa F, Ginzburg D, Meo M 2015 *SPIE Proc. 9437* **943706**

[29] Amerini F, Meo M 2011 *Struct. Health Monitor.* **10** 659-72

[30] Kawashima K, Omote R, Ito T, Fujita H, Shima T 2002 *Ultrasonics.* **40** 611-15

[31] Biwa S, Hiraiwa S, Matsumoto E 2006 *Ultrasonics.* **44** 1319-22

[32] Lee TH, Jhang KY 2009 *NDT&E Int.* **42** 757-64

[33] Yang Y, Ng CT, Kotousov A, Sohn H, Lim HJ 2018 *Mech. Syst. Signal. Process.* **99** 760-73

[34] Lim HJ, Song B, Park B, Sohn H 2015 *NDT&E Int.* **73** 8-14

[35] Lin X, Yuan FG 2001 *Smart Mater. Struct.* **10** 907-13

[36] Su Z, Ye L 2005 *J. Intel Mater. Syst. Struct.* **16** 97-111

[37] Blau PJ 2009 *Friction Science and Technology: from concepts to applications* (Boca Raton: CRC Press)

[38] Sohn H, Lee SJ 2009 *Smart Mater. Struct.* **19** 015007

[39] Giurgiutiu V 2005 *J. Intel. Mater. Syst. Struct* **16** 291-305

[40] Lu Y, Ye L, Su Z, Yang C 2008 *NDT&E Int.* **41** 59-68

[41] Mohabuth M, Kotousov A, Ng CT 2016 *Int. J. Non-Linear Mech.* **86** 104-11